npj Computational Materials

www.nature.com/npjcompumats

ARTICLE OPEN

Check for updates

Microstructural impacts on ionic conductivity of oxide solid electrolytes from a combined atomistic-mesoscale approach

Tae Wook Heo[1,5✉], Andrew Grieder[2,5], Bo Wang[3], Marissa Wood[1], Tim Hsu[4], Sneha A. Akhade[1], Liwen F. Wan[1], Long-Qing Chen[3], Nicole Adelstein[2✉] and Brandon C. Wood[1✉]

Although multiple oxide-based solid electrolyte materials with intrinsically high ionic conductivities have emerged, practical processing and synthesis routes introduce grain boundaries and other interfaces that can perturb primary conduction channels. To directly probe these effects, we demonstrate an efficient and general mesoscopic computational method capable of predicting effective ionic conductivity through a complex polycrystalline oxide-based solid electrolyte microstructure without relying on simplified equivalent circuit description. We parameterize the framework for $Li_{7-x}La_3Zr_2O_{12}$ (LLZO) garnet solid electrolyte by combining synthetic microstructures from phase-field simulations with diffusivities from molecular dynamics simulations of ordered and disordered systems. Systematically designed simulations reveal an interdependence between atomistic and mesoscopic microstructural impacts on the effective ionic conductivity of polycrystalline LLZO, quantified by newly defined metrics that characterize the complex ionic transport mechanism. Our results provide fundamental understanding of the physical origins of the reported variability in ionic conductivities based on an extensive analysis of literature data, while simultaneously outlining practical design guidance for achieving desired ionic transport properties based on conditions for which sensitivity to microstructural features is highest. Additional implications of our results are discussed, including a possible connection between ion conduction behavior and dendrite formation.

npj Computational Materials (2021)7:214 ; https://doi.org/10.1038/s41524-021-00681-8

INTRODUCTION

Solid electrolytes offer promise for overcoming key technological hurdles associated with the narrow electrochemical and thermal stability windows of conventional Li-ion and Na-ion batteries using organic liquid-based electrolytes. Recently, many studies have reported solid-state inorganic electrolytes exhibiting comparably high ionic conductivity at room temperature (>1 mS cm^{-1}), including various ceramic oxides, sulfides, halides, and complex-anion salts[1–5]. Accordingly, a variety of experimental and computational approaches have been utilized to investigate ionic transport mechanisms in these fast ionic conductors[6]. However, ionic transport kinetics in these materials are highly sensitive to the topological characteristics of the ion conduction pathways. As a result, microstructural features that appear unavoidably in practical solid-state materials—including defects, structural disorder, and networks of internal interfaces—have a significant impact on the actual transport properties. They also introduce inhomogeneity in mechanical properties, which, in addition to impacting lithium dendritic growth[7,8], may have a nontrivial secondary coupling to ionic diffusion mechanisms. In general, a better understanding of the detailed relationship between microstructure and diffusion is critical to developing synthesis and processing pathways for viable solid electrolyte materials that retain high ionic conductivity, since these pathways typically determine microstructural characteristics.

Among the various solid electrolyte candidates considered to date, one of the most widely studied oxide-based electrolytes is the $Li_7La_3Zr_2O_{12}$ (LLZO) garnet system, which exhibits excellent thermal stability and mechanical stiffness, as well as stability against a Li metal anode[9]. The material is commonly doped (e.g., with Al or Ta) to stabilize the conductive cubic phase[3,4,10–13]. However, LLZO is also a brittle ceramic that is typically processed via particle sintering, generating a variety of microstructures with features that depend on the specific processing temperature and packing conditions[9,14–16]. The role of resulting grain boundaries and other microstructural factors in determining LLZO ionic conductivity remains under debate. For example, the material exhibits a wide range of literature-reported room-temperature ionic conductivity values, pointing to its strong dependence on microstructure[4,5,9,14–16]. However, this connection cannot be definitely established, and alternative explanations have been invoked to explain the variations[9]. It is generally believed that grain boundaries in LLZO inhibit ionic transport by disrupting conduction channels present in the crystalline regions. On the other hand, it has also been reported that grain boundaries may have faster ionic transport pathways at room temperature, according to the grain versus grain boundary contributions to ionic conduction from electrochemical impedance spectroscopy[15]. In addition, experimentally observed Li dendrite growth along grain boundaries[17] indicates possible dominant ionic conduction through grain boundaries. These disagreements highlight the need for a more systematic approach to understanding the role of microstructure in Li^+ ionic conduction in LLZO.

The complexity of microstructural features in solid electrolytes introduces significant challenges for directly characterizing the relationship between microstructure and ionic conductivity within operating environments. The most common approach involves decoupling different contributions from electrochemical

[1]Materials Science Division, Lawrence Livermore National Laboratory, Livermore, CA 94550, USA. [2]Department of Chemistry and Biochemistry, San Francisco State University, San Francisco, CA 94132, USA. [3]Department of Materials Science and Engineering, The Pennsylvania State University, University Park, PA 16802, USA. [4]Center for Applied Scientific Computing, Lawrence Livermore National Laboratory, Livermore, CA 94550, USA. [5]These authors contributed equally: Tae Wook Heo, Andrew Grieder. ✉email: heo1@llnl.gov; nicoleal@sfsu.edu; wood37@llnl.gov

Published in partnership with the Shanghai Institute of Ceramics of the Chinese Academy of Sciences

npj nature partner journals

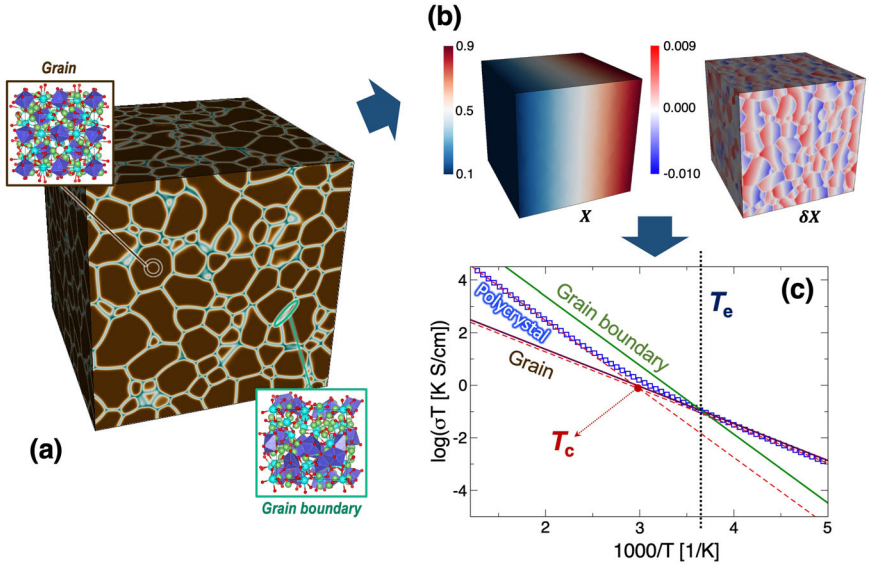

Fig. 1 Computational procedure for extracting effective ionic transport properties of complex oxide microstructures. a Example digital representation of a polycrystalline LLZO microstructure, incorporating crystalline grains and atomistically disordered grain boundaries; **b** steady-state profile of Li composition (X) along with its perturbation part (δX) (see Eq. (6) in Methods) within the example microstructure; and **c** extracted effective ionic conductivity as a function of temperature. For bulk and grain boundary diffusivities, values of $D_0^{bulk} = 3.72\times10^{-4}\,cm^2\,s^{-1}$, $E_a^{bulk} = 0.28\,eV$, $D_0^{gb} = 1.00\times10^{1}\,cm^2\,s^{-1}$, and $E_a^{gb} = 0.52\,eV$ were assumed. The equivalent temperature at which the grain boundary and grain conductivities are equal is denoted by T_e, while the critical temperature at which the transition from grain- to grain boundary-dominated conduction occurs is denoted by T_c.

impedance spectroscopy. However, the results depend on the specific equivalent-circuit model employed, and separation can be nontrivial if both grain boundaries and grains provide accessible conduction pathways. The simplest circuit model involves separate interfacial/grain boundary and bulk conduction channels operating in parallel, but this is not representative of the actual topology of the ionic transport channels and neglects local concentration gradients that form due to structural and diffusional inhomogeneities. A far more attractive alternative is to employ a direct simulation framework that can systematically vary independent microstructural features and assess their individual impacts on the effective ionic conductivity through the polycrystalline material. In principle, a reliable model should operate across the relevant length and time scales to resolve diffusion paths through the crystalline domains and within the boundary regions under a macroscopic concentration gradient, while simultaneously considering secondary factors such as diffusive segregation to boundary regions and competitive interchange between grain and boundary conduction modes.

The present work combines a broad suite of multiscale simulation capabilities to address this key knowledge gap. First, we introduce a numerically efficient and flexible modeling framework capable of directly mimicking the steady-state current response through an arbitrary complex microstructure. Next, extensive molecular dynamics simulations of crystalline and disordered regions are used to parameterize the framework for the specific case of polycrystalline LLZO, providing the necessary fidelity to resolve diffusivity differences associated with structural disorder. Finally, we use phase-field simulations to generate systematically varied microstructures for assessing the sensitivity of effective ionic conductivity to specific features. We conclude that mesoscopic grain structure and atomistic grain boundary structures are indeed highly relevant to determining overall ionic conduction in LLZO and that the transition between grain- and grain-boundary-dominated conduction mechanisms can be used as a guide for engineering LLZO microstructures for optimal transport. The results provide key missing insights into the relationship between processing and performance in ceramic solid electrolytes.

RESULTS

Mesoscale model for effective ionic conductivity

Our computational framework probes the relationship between solid electrolyte microstructure and effective ionic conductivity by integrating mesoscale and atomistic simulations, as illustrated in Fig. 1. We first employ a phase-field grain growth model[18,19] to generate a model LLZO microstructure, with Li^+ diffusivities within the grains and grain boundaries parameterized by molecular dynamics simulations (Fig. 1a). We then numerically obtain a steady-state Li^+ concentration profile over the generated synthetic microstructure under a macroscopic concentration gradient (Fig. 1b), from which the effective ionic conductivity is extracted (Fig. 1c). We point out that a few microstructure-level modeling efforts for polycrystalline solid electrolytes have been reported previously, either based on the equivalent circuit model or direct mass transport simulations[20–22]. Note that our established methodology incorporates advantages of both approaches; it maintains numerical efficiency without oversimplifying complex features of a realistic microstructure. A similar approach has been applied to a different material system[23]. This multiscale scheme enables efficient exploration of a wide range of the parameter space associated with microstructural topology and operating temperature, leading to a comprehensive assessment of the relationship between microstructure and ionic transport property. The following subsections describe this methodology in detail.

Generation of realistic LLZO microstructures. Experimentally fabricated LLZO solid electrolytes are generally polycrystalline, containing multiple grains separated by grain boundaries. Therefore, a practical LLZO sample incorporates a spatially non-uniform microstructure that depends on the specific processing conditions. Moreover, the available diffusion pathways within the microstructure exhibit a complex topology due to the non-trivial connectivity of grain boundaries, making it critical to consider a

realistic LLZO microstructure in computing the effective Li^+ diffusivity. To explore the fundamental microstructural impacts of polycrystalline LLZO, we used a phase-field grain growth model[18,19], which is widely accepted to reproduce experimentally relevant topological features, to generate generic yet realistic digital representations of synthetic grain structures with systematically varied average grain sizes, grain boundary widths, and grain morphologies. The phase-field formalism is based on the diffuse-interface theory[24,25]. It provides a convenient recipe for controlling key topological features by altering the governing parameters (for instance, the grain boundary width is proportional to the square root of the gradient energy coefficient). In addition, the diffuse-interface nature of the model incorporates a more natural description of a grain boundary at the mesoscale in comparison with sharp-interface-based models. Further details on the model can be found in Supplementary Note 1. Supplementary Fig. 1 shows examples of generated digital LLZO grain structures, which closely resemble literature reports of experimental LLZO microstructures[16,26–28]. We emphasize that because the primary focus of this work is to evaluate the variability of ionic transport with microstructure, it is critical that we utilize a method capable of systematically controlling the microstructural features in our modeling framework. For this purpose, it is sufficient to employ a non-dimensionalized descriptive model. The LLZO-specific information is therefore introduced through the position-dependent diffusivity model described in 'Computation of effective conductivity' subsection and 'Parameterization of local mobility' section. Although it is not the focus of the current work, it should be possible to further connect sintering processing conditions and actual LLZO microstructure evolution using advanced phase-field sintering models[29–32] or other refined microstructure simulations.

To characterize the generated microstructures, we introduce dimensionless quantities $\widetilde{\langle d \rangle}$ and $\widetilde{\langle l_{gb} \rangle}$ to represent grain size and grain boundary width, respectively. These are defined as relative ratios $\langle d \rangle / \langle l_{gb} \rangle$ and $\langle l_{gb} \rangle / \langle d \rangle$, respectively, where $\langle d \rangle$ is the average grain size and $\langle l_{gb} \rangle$ is the average grain boundary width defined within the computational domain. The ratio is a convenient metric for comparing relative grain size and grain boundary width. These are especially advantageous to use when the actual length scales of the related microstructural variables are not well verified. Specifically, the accurate measurement of grain boundary width is extremely challenging, leading to inconsistency in experimental characterizations. Although a few experimentally characterized LLZO grain boundary widths have been reported[11,33], these have mostly focused on well-defined or dense grain boundaries. More generic LLZO grain boundaries have not been extensively characterized to our knowledge. Therefore, by employing the dimensionless relative ratios, we may systematically investigate the microstructural impact by independently examining the effect of each upon fixing the other without arbitrarily or unphysically defining physical length scales. Note that these quantities can be easily converted to actual scales once a physical scale of one size parameter (i.e., $\langle d \rangle$ or $\langle l_{gb} \rangle$) is identified. Moreover, it is worth pointing out that the grain boundary width emulated in our diffuse-interface formalism should be effectively thicker than the structural disorder might indicate since we consider grain boundaries as ionic diffusion channels, which should account for any space charge layer present near grain boundaries that extends some distance into the grains[34–36].

Computation of effective conductivity. In a single-ion conductor, the relationship between Li^+ ionic conductivity (σ) and diffusivity (D) can be approximated from molecular dynamics by the Nernst-Einstein equation[37]:

$$\sigma \approx D \cdot ce^2/(Hk_BT), \tag{1}$$

where c is the Li^+ concentration, e is the elementary charge, k_B is the Boltzmann constant, T is temperature, and H represents the Haven ratio[38] that incorporates effects of directional correlation (set to unity in this study for convenience). This indicates that the overall Li^+ ionic conductivity in polycrystalline LLZO can be characterized by evaluating its effective diffusivity through the complex microstructure, which can be extracted by establishing a steady-state profile of the Li^+ concentration field under a macroscopic Li concentration gradient[39,40]. Specifically, we numerically solve the steady-state diffusion equation:

$$\nabla_i \cdot \left[D_{ij}(\vec{\mathbf{r}})\right] \nabla_j X(\vec{\mathbf{r}}) = 0, \tag{2}$$

where D_{ij} is the Li^+ diffusivity tensor and X is the Li^+ composition field, both of which carry spatial dependence. For convenience, we define the composition X as a normalized quantity y/y_{max}, where y is the local atomic fraction of Li^+ ($=(7-x)/(24-x)$ for $Li_{7-x}La_3Zr_2O_{12}$) and y_{max} is the maximum atomic fraction of Li^+ ($=7/24$ for stoichiometric $Li_7La_3Zr_2O_{12}$). In fact, the diffusivity tensor in Eq. (2) ought to be a chemical diffusivity (D_{ij}^{chem}) due to the composition gradient. However, for simplicity, we assume the spatially constant thermodynamic factor (I) for Eq. (2). By doing so, the constant I can be cancelled out, considering the relationship between the self-diffusivity (D_{ij}) and chemical diffusivity: $D_{ij}^{chem} = D_{ij} \cdot I$, resulting in the steady-state equation with the self-diffusivity. Therefore, the self-diffusivity derived from molecular dynamics simulations can be directly used for the equation. The complex microstructural information is incorporated in $D_{ij}(\vec{\mathbf{r}})$, which in turn poses numerical challenges for solving Eq. (2). To overcome these numerical challenges, we employ the mathematically flexible and numerically efficient Fourier-Spectral Iterative Perturbation Method (FSIPM) for mass transport equations[23,39–41]. Numerical details can be found in Methods.

To account for local variation, we employ a generic position-dependent diffusivity model as

$$D_{ij}(\vec{\mathbf{r}}) = g(\{\xi_g\}) D_{ij}^{bulk} + \left[1 - g(\{\xi_g\})\right] D_{ij}^{gb}, \tag{3}$$

where D_{ij}^{bulk} is the bulk (or grain interior) diffusivity, D_{ij}^{gb} is the grain boundary diffusivity, $\{\xi_g\}$ represent phase-field variables that characterize an LLZO grain structure, and $g(\{\xi_g\})$ is an interpolation function. The diffusivities of bulk ($D_{ij}^{bulk}(T)$) and grain boundaries ($D_{ij}^{gb}(T)$) are temperature dependent, given by the Arrhenius forms:

$$\begin{aligned} D_{ij}^{bulk}(T) &= D_{ij}^{bulk,0} \exp\left[-E_a^{bulk}/(k_BT)\right], \\ D_{ij}^{gb}(T) &= D_{ij}^{gb,0} \exp\left[-E_a^{gb}/(k_BT)\right], \end{aligned} \tag{4}$$

with prefactors $D_{ij}^{bulk,0}$, $D_{ij}^{gb,0}$ and activation energy barriers E_a^{bulk}, E_a^{gb}. Note that the interpolation function $g(\{\xi_g\})$ naturally carries the information about how the diffusivity profile varies across each grain boundary, implicitly incorporating local structural and topological variabilities. For this work, we mainly choose the following smooth interpolation function:

$$g(\{\xi_g\}) = \left(\sum_g \xi_g^2 - \phi_{min}\right)/(\phi_{max} - \phi_{min}), \tag{5}$$

where $\phi_{max} = \max(\sum_g \xi_g^2)$ and $\phi_{min} = \min(\sum_g \xi_g^2)$. This function becomes unity within grains, less than unity within grain boundary regions, and zero at the center of grain boundaries. We note that the choice of $g(\{\xi_g\})$ is not unique; step functions or other types of functions can also be employed depending on the purpose of simulations. Further details of the numerical verification and validation of our methodology can be found in Supplementary Note 2. In addition, the variability of $g(\{\xi_g\})$ and

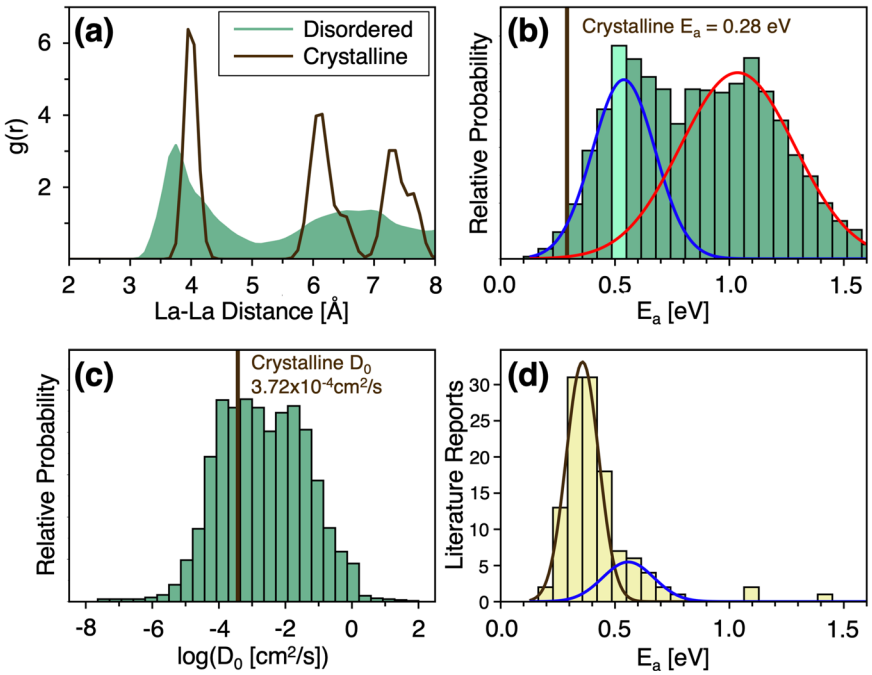

Fig. 2 Atomistic simulations of grain and grain boundary diffusion. a Comparison of La-La pair distribution function, $g(r)$, for $Li_{6.25}La_3Zr_2O_{12}$ at 700 K between the crystalline cubic structure and a representative disordered model ($\rho = 4.77\ g\ cm^{-3}$), showing the breakdown of long-range order for the disordered representation of high-angle grain boundaries. **b**, **c** Normalized histograms of **b** E_a and **c** log (D_0) for individual Li^+ comprised of all disordered models for $Li_{7-x}La_3Zr_2O_{12}$ with $x = 0.25$, 0.50, and 0.75 (see Supplementary Note 3 for details). The computed E_a and D_0 for cubic $Li_{6.25}La_3Zr_2O_{12}$ are labeled as brown vertical lines in **b**, **c**. The mode of the E_a histogram is highlighted in **b** and corresponds to 0.52 eV, near the center of the lower-energy peak (blue). **d** Histogram of experimental LLZO E_a values reported in the literature, taken from the references in Supplementary Table 3 of Supplementary Note 4.

its impacts on the effective ionic diffusivity were discussed in the same section.

For a given polycrystalline LLZO microstructure, we computed the effective ionic diffusivities for many sampled temperatures and converted them to ionic conductivities according to Eq. (1). Figure 1c shows an example of the computed effective conductivity for the microstructure in Fig. 1a. It is worth emphasizing that our formalism implicitly captures the impact of heterogeneity on effective ionic conductivity at both the atomic and microstructural scales, pointing to different engineering strategies at the two scales that ultimately manifest in the effective ionic conductivity. Although the primary focus of this paper is microstructural engineering, we also introduce some general principles for parameterizing atomic-scale mobility in the grain boundaries and understanding its impact on the overall ionic transport property of a given microstructure.

Parameterization of local mobility

Although the modeling framework for effective ionic conductivity as a function of microstructure is general, the detailed implications depend on the parameters used to describe ion mobility in the grain and grain boundary regions. Parameterization based on fitted electrochemical impedance spectra is possible but introduces an artificial sensitivity to the choice of the circuit model, the physical origin of which is often uncertain. In addition, values can vary widely depending on processing, measurement, and/or sample conditions[42–46] (also see Supplementary Table 3 and references therein for a comprehensive survey of the variability of reported diffusion measurements of LLZO formulation). In the absence of an unbiased reference data set, we instead extract our initial diffusion parameters directly from molecular dynamics (MD) simulations to determine realistic ranges of grain boundary diffusion mobilities (see Methods for details). In addition to decoupling our predictions from equivalent-circuit assumptions, this fully predictive, multiscale formalism permits unbiased exploration of a wider variety of possible effects of microstructure on ionic conductivity, with a view towards identifying potential engineering strategies.

Bulk diffusivity parameters were obtained from our MD simulations of the composition for $Li_{6.25}La_3Zr_2O_{12}$, which corresponds roughly to the composition from common levels of Al doping in LLZO[11,15,47]. For the crystalline grain regions, we first performed Arrhenius analysis of molecular dynamics simulations of cubic LLZO. We obtained an activation energy barrier of $E_a^{bulk} = 0.28$ eV and a diffusion prefactor of $D_0^{bulk} = 3.72 \times 10^{-4}\ cm^2\ s^{-1}$ (indicated with brown lines in Fig. 2b, c). These values are in good agreement with literature reports from previous classical and first-principles simulations[12,48–50]. Our data are also in harmony with a statistical representation of available experimental results, as seen in Fig. 2d. The broad range of these literature reports (tabulated in detail in Supplementary Table 3) prevents fair validation by comparing individually selected data points. However, we can fit the ensemble of reported experimental E_a values with a bimodal Gaussian distribution (Fig. 2d). The lower-energy peak, which in polycrystalline samples is presumably dominated by the bulk grain conduction, is centered around 0.35 eV and encompasses our MD value for E_a^{bulk}.

Unlike crystalline grains, it is far more difficult to assign precise values to the grain boundary regions due to individual variations in atomic structure, misorientation, density, and composition. Moreover, whereas fast diffusion in a cubic LLZO grain is thought to occur via collective ion motion through well-defined channels of tetrahedral and octahedral sites[48], such channels are absent or ill-defined in grain boundary regions, leading to a qualitatively different diffusion mechanism and thus significantly different regional diffusion behavior with varying temperature.

Previous simulation work by Yu and Siegel explored specific ordered tilt grain boundary structures in LLZO, including the

low-energy Σ5 (210) and (310) boundaries[49], which exhibited diffusion barriers higher than their bulk counterparts. Additional work by Zhu examined twist boundaries, which were also shown to slow diffusion[51]. In both cases, these symmetric grain boundary diffusivities were computed to be within an order of magnitude of the bulk[49,51], suggesting they may compete with the grains to determine ionic conductivity at operating temperatures. Nevertheless, the actual barriers differed significantly in the two studies. Recently, Shiiba *et al*. discussed the effects of more general cases of symmetrically tilted grain boundaries on Li^+ ion conduction[52]. In addition, low-angle grain boundaries incorporate an array of dislocations[53], which can alter ionic diffusion mechanisms. Chemical defects could likewise impact ionic conductivity. Such defect could include impurities or intentionally introduced dopants, including those commonly incorporated into LLZO to stabilize the more conductive cubic phase, enhance ionic conductivity, or control the sintering temperature[10–13]. Oftentimes, these chemical species can segregate to grain boundaries or promote formation of new interfacial phases, significantly affecting ionic diffusion in these boundary regions[54–56]. Overall, the diversity of the available data emphasizes the need to consider a wider variety of possible grain boundary configurations within a more general computational approach.

Furthermore, the necessity for a more general approach that can incorporate disordered and high-angle grain boundaries is apparent from electron backscatter diffraction studies of various LLZO microstructures, which have shown a broad and continuous distribution of misorientation angles between 0 and 60°, with little preference for any particular type of grain boundary orientation in pressed and calcined samples[16].

As grains grow under high temperature (1100–1300 °C) hot pressing, these distributions change, but no preference for the lowest-energy orientational interfaces emerges. Moreover, transmission electron microscopy (TEM) images suggest grain boundary thicknesses of ~2 nm[11,33], consistent with loss of lattice coherency across grain boundaries.

In light of these observations, we adopted a series of randomly disordered atomistic models for the grain boundary region, each of which generated by quenching from melt simulations hot enough to introduce significant disorder in the La and Zr environments while cool enough to retain local cation-oxygen structural moieties. Two different densities and three different Li^+ compositions were tested to mimic the variability in these quantities across individual grain boundaries and different processing conditions (see Methods and Supplementary Note 3 for details on how these models were created and a summary of the key structural characteristics). Figure 2a compares the La-La pair distribution function (PDF) from one representative disordered LLZO model with the crystalline (ordered) counterpart; examples of the corresponding atomic structures can be found in Fig. 1a. Additional PDFs for all atomic pairs in all disordered simulations are also presented in Supplementary Fig. 4 in Supplementary Note 3, alongside analogous results for the crystalline and melted systems. Our array of models captures the structurally disordered nature of the incoherent interfaces[57–59] and can be considered broadly representative of generic single-phase, high-angle grain boundaries.

Results for the values of E_a and D_0 extracted from the disordered models are shown in Fig. 2b, c. Conventionally, these parameters would be obtained from Arrhenius fits after averaging across all Li^+ ions. However, this convention belies the fact that unlike crystalline materials, disordered variants contain a variety of possible site geometries and local atomic arrangements. This variability leads to a dispersion of diffusion timescales for individual ions, the collective result of which comprises the overall diffusion behavior. Accordingly, in any finite simulation, the behavior is not fully ergodic, and simple averages converge too slowly to adequately encompass the sampling of possible values of E_a or D_0 experienced by diffusing Li^+ at any given time or site. To overcome this limitation, we introduce an alternative approach that tracks 'local' E_a and D_0 values by performing Arrhenius analysis for each individual diffusing ion. This analysis was applied to all disordered models across multiple densities and compositions, and results were collected into single statistical distributions for E_a and D_0. These distributions implicitly describe the heterogeneity of diffusion pathways and local environments explored within the dynamics, incorporating effects of structure, composition, and density variation across the various structural models. We point out that high variability of conductivity has even been observed within a single polycrystalline sample, confirming that individual grain boundaries exhibit a breadth of local properties[46]. This is best accounted for by adopting a statistical approach, as we introduce here.

The distribution of activation energy barriers E_a for the disordered simulations exhibits a broad bimodal distribution spanning values from ~0.1 to ~1.9 eV (see Fig. 2b), reflecting the diversity of possible local environments. We note that the Gaussian fit (blue) of the lower E_a peak from MD (Fig. 2b) overlaps with the Gaussian distributions from our collection of literature values (Fig. 2d). The mode of the overall distribution lies at 0.52 eV (indicated with light green in Fig. 2b) near the center of the lower-energy peak. Notably, the disordered simulations values are generally much higher than for crystalline LLZO (vertical line in Fig. 2b), in agreement with the generally accepted notion that the grain boundaries can inhibit ionic conductivity in LLZO[9,11,15,60,61]. The bimodal shape of the E_a distribution reflects the simultaneous presence of 'fast' and 'slow' conduction channels in the disordered regions, similar to those reported previously for Li^+ diffusion in amorphous TiO_2[62]. Based on the MD trajectories for the slower-diffusing ions, we conclude that the higher E_a distribution centered at ~1.1 eV represents 'trap' sites with high escape barriers. It is worth exploring how our distribution compares to previous simulation results on symmetric tilt and twist grain boundaries. For twist boundaries, Zhu reported an E_a value of 0.36 eV[51], whereas for tilt boundaries, Yu and Siegel reported values between 0.52 eV and 0.71 eV depending on the specific orientation[49]. In both cases, these values were higher than the values for the crystalline bulk, indicating a propensity for disrupting beneficial correlated Li^+ motion. The high-angle grain boundaries mimicked by our approach generally have lower densities and greater disorder, which leads to a broader distribution of activation energy barriers; nevertheless, it is notable that the previous simulation results for more ordered boundaries also lie within our computed distribution. A more detailed analysis of the impact of atomic-scale disorder on diffusion pathways and mechanisms will be presented in a forthcoming publication.

The distribution of individual D_0 values (see Fig. 2c) is similarly broad, spanning several orders of magnitude from ~10^{-6} to ~10^{1} $cm^2\ s^{-1}$ (here, the bimodality is less evident). Overall, the D_0 values also tend to exceed those of crystalline LLZO (vertical line in Fig. 2c). The ranges of E_a and D_0 reported in Fig. 2 encompass the realistic ranges of parameters that could be achieved depending on processing conditions, as shown through comparison with E_a literature values in Fig. 2d. The data and references used to generate Fig. 2d are given Supplementary Table S3 in Supplementary Note 4. Accordingly, these ranges were used as a basis for exploring the sensitivity of overall effective ionic conductivity to grain boundary diffusivity parameters E_a^{gb} and D_0^{gb}.

As a first step in our analysis, we select a baseline case of parameters for the grain boundaries that can be used to explore qualitative trends in microstructure. Following our discussion of general trends using the baseline parameterization, we will proceed to investigate a more complete range of possible values and incorporate the results of the atomistic E_a^{gb} and D_0^{gb} distributions more directly. The mode of the E_a^{gb} distribution was selected for initial analysis (0.52 eV), as this value best captures the 'fast' diffusion channel. In the grain boundaries, we may safely assume that

diffusion pathways with higher-barrier trap sites (red distribution in Fig. 2b) are infrequently used for diffusion. As a result, the 'fast' diffusion channel should dominate the kinetics as long as a percolating network of low-barrier pathways is accessible, as should be the case for the relatively thin grain boundaries[62,63]. As further justification, we note that the computed distribution of E_a^{gb} from 'fast' channels is an excellent match to the higher-barrier feature in the experimental E_a distribution, which contains contributions from the grain boundaries. We point out that in the two previous computational studies of symmetric tilt and twist grain boundaries[49,51], the grain boundary contribution to the effective diffusivity would be more significant due to the smaller difference in E_a between the grains and grain boundaries; this likely reflects the lower degree of disorder and higher density in these models compared to our models. For the baseline value of D_0^{gb} in our initial analysis, we selected 10^1 cm^2/s, which lies near the upper edge of our computed distribution. This choice can be considered a 'best-case' scenario that best magnifies the sensitivity of the ionic conductivity to microstructure at experimentally relevant temperatures.

Ionic conductivity of polycrystalline LLZO

Combining the digitally generated representations of polycrystalline LLZO microstructures, the established mesoscale model, and the derived Li^+ diffusivities from the atomistic simulations, we proceed to compute effective ionic conductivities. Our analysis focuses on the impacts of atomic-scale grain boundary properties and mesoscale microstructural features.

Figure 1c shows an example of the computed effective ionic conductivity (*i.e.*, $\log(\sigma T)$ *vs.* $1000/T$). Our simulations show evidence of possible non-Arrhenius behavior, transitioning between high-temperature and low-temperature linear regimes with ionic conduction activation barriers. Within the high-temperature regime, the Arrhenius slope of the effectivity conductivity parallels the grain boundary conductivity line, while the low-temperature counterpart parallels the grain conductivity line. To systematically analyze the microstructure-conductivity relationship, we introduce four characteristic quantities that comprehensively capture the major temperature-sensitive features of the computed effective conductivity: (i) an equivalent temperature (T_e) at which the intrinsic ionic conductivities of grain and grain boundaries are equal; (ii) a critical temperature (T_c) representing the transition point between grain- and grain boundary-dominated conduction mechanisms (see Fig. 1c for visual definition of T_e and T_c, as well as Methods for more details of mathematical/numerical procedures for determining the two temperatures); (iii) the effective ionic conductivities at $T_L = 250$ K and $T_H = 450$ K representing plausible limits of battery operation; and *iv*) the mean effective diffusion prefactor ($\overline{D}_0^{eff}$) and activation energy ($\overline{E}_a^{eff}$) obtained from Arrhenius analysis of the effective ionic conductivity over the temperature range $T_L \le T \le T_H$, using the linear least square fitting method. It is important to distinguish T_c and T_e. Whereas T_e is an intrinsic characteristic temperature that depends on the atomic-scale character of the grain boundaries, T_c is sensitive to the relative contributions from grains and grain boundaries and thus highlights information about the microstructure.

Variability of ionic conductivity by tuning atomic grain boundary structure. We begin by exploring the impact of grain boundary diffusion on the effective ionic transport properties of LLZO. The specific atomic structure of the grain boundary is sensitive to processing conditions. As discussed in 'Parameterization of local mobility' section, the grain boundary diffusion exhibits large variability due to the local atomic structure. Yu and Siegel[49] has also verified similar effects, showing that the activation energy (E_a^{gb}) for diffusion can be lower for low-angle, highly ordered grain boundaries, which may have increased relevance upon low-temperature annealing. Similarly, it is easy to imagine that the corresponding prefactor (D_0^{gb}) could exhibit significant variability with the atomic structure of the grain boundaries because it depends on potential lithium segregation to the grain boundaries, as well as the connectivity of available diffusion pathways at the interface. A detailed study of the specific atomic arrangements at grain boundaries is in practice challenging to achieve given the high variability of misorientation angles and difficulties in characterizing atomic-level structures. However, we can indirectly probe their collective impact on effective ionic transport by instead varying E_a^{gb} and D_0^{gb} as proxies for disordered structures with different stoichiometry and density. As discussed above, practically possible ranges for these diffusion parameters were selected from the results of our molecular dynamics simulations. Figure 3 shows the results for polycrystalline LLZO under independent variation of activation energy E_a^{gb} (Fig. 3a) and prefactor D_0^{gb} (Fig. 3b) of grain boundary diffusion, with the other parameter fixed. In each case, the grain size and grain boundary width are held constant ($\langle\widetilde{d}\rangle = 23.5$, see Supplementary Fig. 1 in Supplementary Note 1 for the corresponding grain structure), and the results are compared to the single-crystal bulk reference. As expected, smaller values of E_a^{gb} and larger values of D_0^{gb} lead to more significant deviations from the single-crystal behavior at the warmer end of the temperature range due to the larger contribution of competing grain boundary conduction pathways. At the cooler end of the temperature range, the conductivity lies much closer to the single-crystal value and can actually decrease below this reference value for some combinations of E_a^{gb} and D_0^{gb}, indicating the possibility of blocking tendency by the grain boundaries (see also Supplementary Fig. 3b and relevant text in Supplementary Note 2). Nevertheless, within the temperature range sampled here, the grain boundary contribution has a far smaller effect at low temperatures than at higher temperatures. As a result, we can conclude that the degree to which atomic properties of the grain boundary can affect diffusion itself depends on temperature.

Figure 3a highlights a relevant temperature window within which the overall microstructure-dependent ionic conductivity exhibits the most appreciable sensitivity to the specific diffusion properties of the grain boundaries, which in turn depends on the processing and composition of the material. At the most extreme values of D_0^{gb} and E_a^{gb} deemed practically realizable within our molecular dynamics analysis, we estimate that the microstructure could impact conductivity by as much as an order of magnitude at 100 °C. This potentially significant effect points to differences in processing as a plausible explanation of the large spread in reported LLZO conductivity values. Similarly, one may assume that these plots represent a rough estimate of the maximum variation in conductivity achievable through engineering of the atomistic grain boundary structure alone.

Variability of ionic conductivity by tuning mesoscopic grain structure. In this subsection, we explore the impacts of altering the microstructure parameterized by grain size, grain boundary width, and grain morphology on the effective ionic transport properties. These mesoscopic microstructural features can be controlled by synthetic thermo-mechanical processing conditions and methods[14,16]. By varying the mesoscopic features of input digital LLZO microstructures, we analyzed the three major characteristics (i.e., (1) T_c; (2) $\sigma_{Li}(T = T_L \text{ or } T_H)$; (3) $\overline{D}_0^{eff}$ and $\overline{E}_a^{eff}$) defined above. As discussed in 'Generation of realistic LLZO microstructures' subsection, we use dimensionless grain size $\langle\widetilde{d}\rangle$ and grain boundary width $\langle\widetilde{l_{gb}}\rangle$ to represent the microstructures. For these calculations, we chose the bulk diffusivity with $E_a^{bulk} = 0.28$ eV,

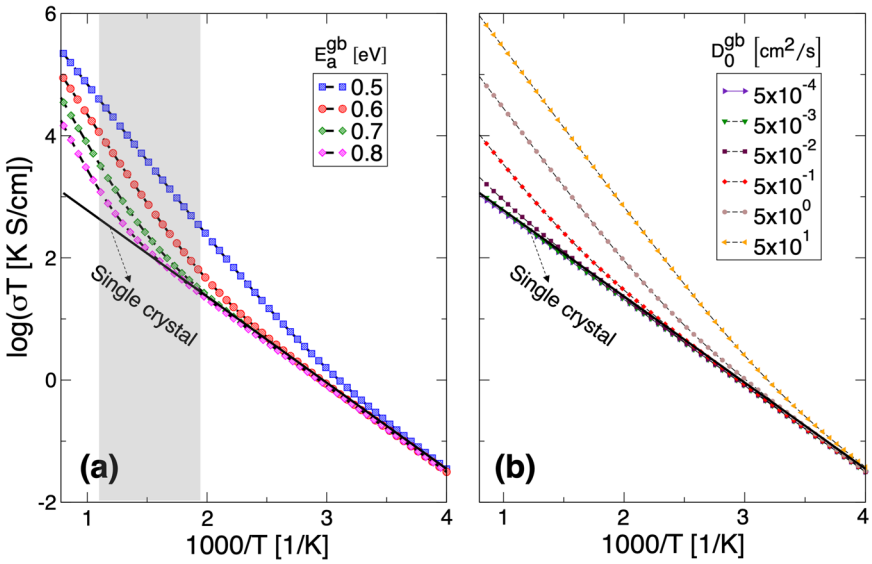

Fig. 3 Variability of the effective ionic conductivity of LLZO due to varied grain boundary properties controlled by their atomistic features. Dependence of the effective ionic conductivity **a** on E_a^{gb} with fixed $D_0^{gb} = 1.0\times 10^1\ cm^2\ s^{-1}$; and **b** on D_0^{gb} with fixed $E_a^{gb} = 0.52\ eV$. Values for the single-crystal reference case are shown by a solid line for comparison. The gray region in **a** represents a relevant operating temperature window for which the effective ionic conductivity exhibits appreciable dependence on the atomic-scale grain boundary properties.

$D_0^{bulk} = 3.72\times 10^{-4}\,cm^2\,s^{-1}$ and the grain boundary diffusivity with $E_a^{gb} = 0.52\,eV$, $D_0^{gb} = 1.00\times 10^1\,cm^2\,s^{-1}$ extracted from our molecular dynamics simulations. We note that the chosen parameters well reproduce similar trends in ionic conductivities for different grain sizes (see Supplementary Fig. 3 in Supplementary Note 2) to experimentally characterized results in the literature[14].

Figure 4a, d show the variation of the analyzed critical temperatures, T_c, versus the grain size and grain boundary width, respectively. According to the figures, T_c varies nonlinearly with the two mesoscopic structural features, increasing as the relative volume of grain boundaries decreases. However, the sensitivity of the variation depends on the microstructural features—T_c is more sensitive to the grain size when grains are small (i.e., more volume of grain boundaries). On the other hand, T_c is more sensitive to the grain boundary width when grain boundaries are thin (i.e., less volume of grain boundaries). As a result, T_c in Fig. 4a, d can be well fitted by a power law relation scaling with $(\langle\widetilde{d}\rangle - d_0)^m$ $(m<1)$ and $(1/\langle\widetilde{l_{gb}}\rangle - 1/l_0)^n$ $(n<1)$, respectively, demonstrating quantitatively characterized dependencies of T_c on the microstructure. We note that although the exponents of the dependencies can vary with the specific grain boundary diffusion properties, a general power law form is always maintained. Accordingly, the behavior of T_c with grain topology may be reasonably predicted by only a few calibration data points representative of the specific electrolyte chemistry and processing mode. Although the fitted power law relation $(T_c = T_e + k(\langle\widetilde{d}\rangle - d_0)^m$ or $T_c = T_e + k(1/\langle\widetilde{l_{gb}}\rangle - 1/l_0)^n$, where k, d_0, l_0 are fitting parameters) as of yet lacks a rigorous physical underpinning, it does have the advantage of separating two key constituents that determine T_c: 1) an intrinsic factor (T_e); and 2) an extrinsic factor ($k(\langle\widetilde{d}\rangle - d_0)^n$ or $k(1/\langle\widetilde{l_{gb}}\rangle - 1/l_0)^n$). As discussed above, T_e is an intrinsic characteristic temperature determined by the Li diffusivities in the grain interior and at grain boundaries. Therefore, the first term of the power law relation for T_c incorporates these intrinsic properties, which are ultimately determined by the atomic-scale characteristics of the material. On the other hand, the second term of the power law relation accounts for the microstructural topology features, which are extrinsically determined at the mesoscale.

Because the mechanistic transition from grain- to grain boundary-dominated transport occurs at T_c, the variation of ionic conductivity with microstructural features depends on the operating temperature. This effect can be clearly seen in Fig. 4b, e, which compare the conductivity trends at T_L (250 K) and T_H (450 K). Note that T_c is located between the two selected temperatures. At T_H ($>T_c$), the grain boundary transport mechanism dominates and the ionic transport along grain boundaries is faster than the bulk counterpart. Therefore, overall conductivity increases with decreased grain size (or increased grain boundary width) since the contribution from the fast-ionic conductive mechanism becomes greater. On the other hand, at T_L ($<T_c$), the bulk transport mechanism dominates over the grain boundary transport. Hence, overall conductivity increases with increased grain size (or decreased grain boundary width); conversely, a blocking effect is observed when a higher fraction of grain boundaries in present. Note that the subtle interdependence implies that the impact of microstructure on ionic conductivity depends not only on the grain features but also on the operating temperature of the solid electrolyte. We speculate that inconsistent ionic conductivity trends with grain sizes in the literature-reported experimental measurements may be caused by choices of different temperature regimes, within which different conduction mechanisms are dominant, for their characterizations.

The mean effective Li^+ transport property over $T_L \le T \le T_H$ is analyzed upon altering grain sizes and grain boundary widths. In particular, we focused on the relationship between $\log\left(\overline{D}_0^{eff}\right)$ and $\overline{E}_a^{eff}$ as shown in Fig. 4c, f. As the grain size increases or grain boundary width decreases, both $\log\left(\overline{D}_0^{eff}\right)$ and $\overline{E}_a^{eff}$ decrease. Because averaging spans a temperature range both below and above T_c, the origin of this behavior should be linked to the transition of ionic transport mechanisms. Therefore, it is reasonable to conclude that the decreasing and increasing trends with grain size and grain boundary width, respectively, are determined by the relative contribution of ionic transport along grain boundaries. Perhaps more intriguingly, in both cases, a clear linear relationship between

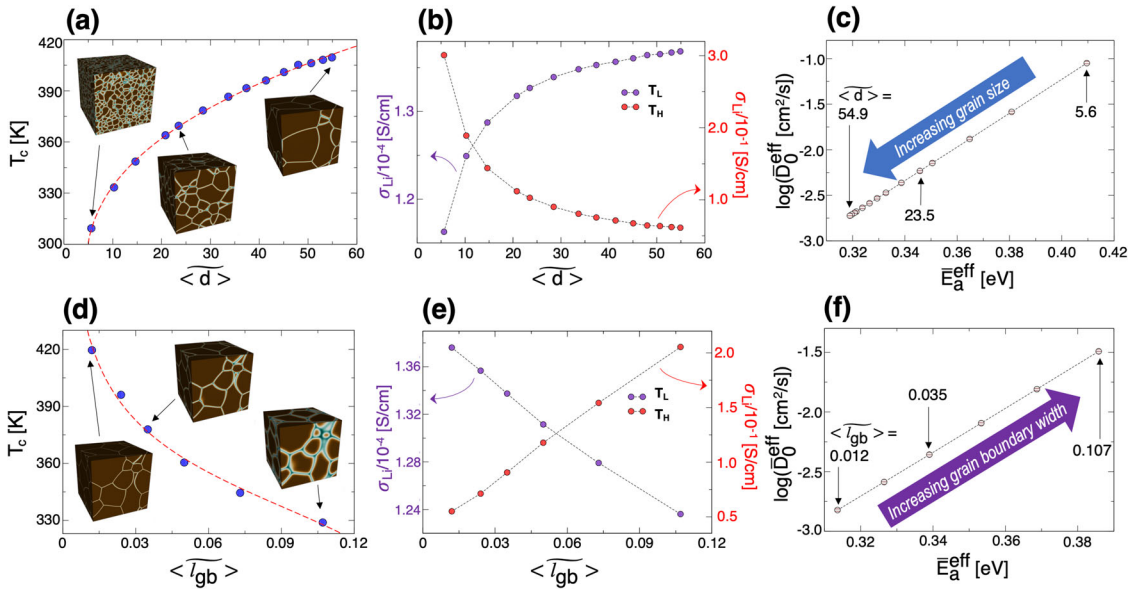

Fig. 4 Variability of effective ionic conductivity properties due to mesoscopic microstructural features. a Computed critical temperature T_c as a function of grain size; **b** effective Li^+ conductivities as a function of grain size at two selected temperatures ($T_L = 250$ K and $T_H = 450$ K); and **c** relation between prefactor and activation energy of the computed effective diffusivity with increasing grain size $\langle \widetilde{d} \rangle$. Specific grain size values are indicated for reference. **d**–**f** Analogous quantities calculated as a function of grain boundary width $\langle \widetilde{l_{gb}} \rangle$. For **a** and **d**, the red dashed lines are fitting curves for the analyzed critical temperatures: $T_c = T_e + 31.4(\langle \widetilde{d} \rangle - 4.2)^{0.378}$ and $T_c = T_e + 42.8(1/\langle \widetilde{l_{gb}} \rangle - 7.0)^{0.287}$, respectively, where T_e is 273.1 K.

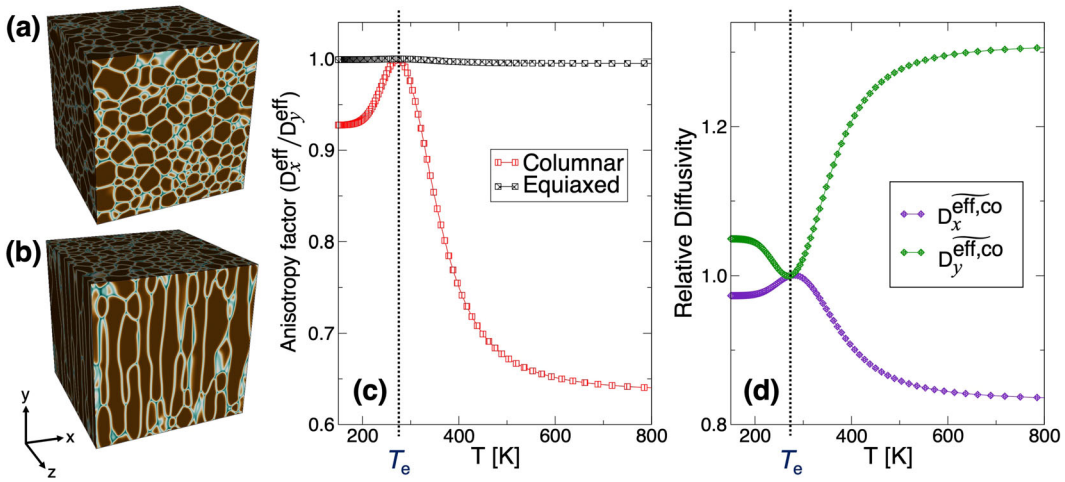

Fig. 5 Impact of grain morphology on effective ionic diffusion property. a Equiaxed LLZO grain structure; **b** columnar LLZO grain structure; **c** analyzed anisotropy factor (D_x^{eff}/D_y^{eff}) as a function of temperature for the two grain structures; and **d** relative diffusivities $D_x^{\widetilde{eff,co}}$ and $D_y^{\widetilde{eff,co}}$ of the columnar grain structure along the x- and y- directions, respectively, as a function of temperature with respect to the isotropic diffusivity of the equiaxed grain structure. The computed equivalent temperature $T_e = 273.1\ K$ for this case is indicated in **c** and **d**.

$\log(\overline{D}_0^{eff})$ and $\overline{E}_a^{eff}$ is preserved as the proportion of bulk and grain boundary conduction is altered. This relationship is well documented in ionic conductors as the so-called Meyer-Neldel rule[64–66], the origin of which has multiple potential attributions. Our results demonstrate that the Meyer-Neldel rule is strictly obeyed for competing ionic transport channels from bulk grains versus grain boundaries at the mesoscopic microstructure-level, providing a means for quickly estimating changes in temperature-dependent ionic conductivity with changes to microstructural features.

Figure 5 shows the impact of grain morphology on the effective ionic diffusivity through application of our method. We employ two limiting cases of grain shape with similar average grain sizes ($\langle \widetilde{d} \rangle \cong 31$): equiaxed (Fig. 5a); and columnar (Fig. 5b) grains. To systematically represent the morphological impact, we first define an anisotropy factor D_x^{eff}/D_y^{eff}, which characterizes the relative diffusivity of Li^+ ions along the *x*-direction to that along the *y*-direction (see orthogonal coordinates in Fig. 5b). As expected, the equiaxed grain structure exhibits the isotropic effective diffusion property

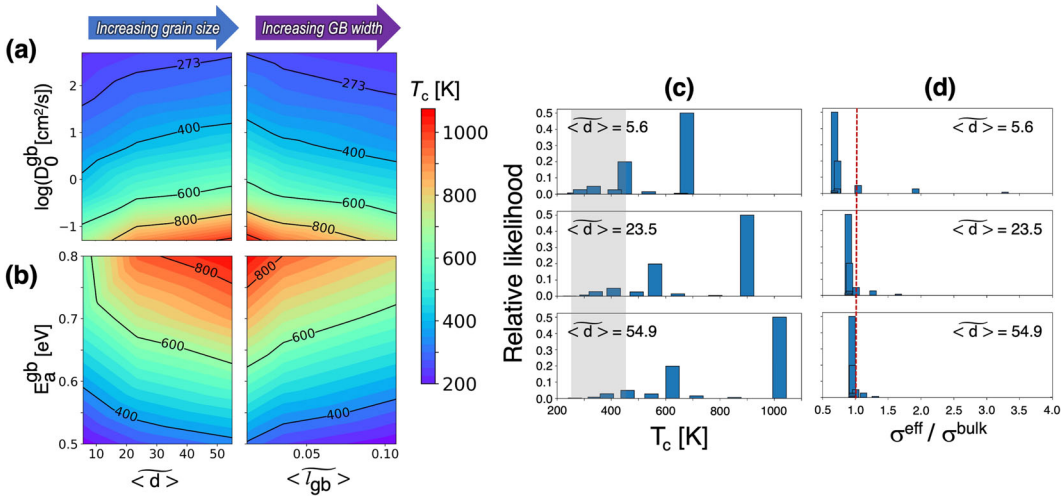

Fig. 6 Designability map of the critical temperature T_c by engineering mesoscopic and atomistic features of polycrystalline LLZO and associated statistical information. Heat map of computed T_c as a collective function of **a** D_0^{gb} and **b** E_a^{gb} with varying grain size (left panels) and grain boundary width (right panels). For **a** and **b**, the corresponding nonvarying quantities E_a^{gb} and D_0^{gb} were fixed at 0.52 eV and 1.0×10^1 $cm^2\ s^{-1}$, respectively. The computed relative likelihood for **c** T_c and **d** $\sigma^{eff}/\sigma^{bulk}$ at 298 K with different grain sizes, based on the data in panels **a** and **b**, weighted according to the relative statistical prevalence in Fig. 2b, c.

(i.e., $D_x^{eff}/D_y^{eff} \sim 1$) over the entire temperature range, as shown in Fig. 5c. On the other hand, effective diffusion through the columnar grain structure is anisotropic. Interestingly, the columnar grain structure exhibits a varying anisotropy factor with temperature, of which the precise character depends on the value of T_e (see Fig. 5c). Specifically, at $T = T_e$, all the diffusivities are equal because $D^{gb} = D^{bulk}$, resulting in $D_x^{eff}/D_y^{eff} = 1$ and a uniform diffusivity profile over the polycrystalline LLZO. At $T < T_e$, the anisotropy appears as the effective diffusivity along the x direction (D_x^{eff}) becomes slightly lower than the y-direction counterpart (D_y^{eff}). On the other hand, the anisotropy is significantly enhanced at higher temperatures ($T > T_e$), with the effective diffusivity along the x-direction reaching ~60% of the y-direction value at the highest simulated temperature.

Figure 5d directly represents the temperature-dependent relative effective Li^+ diffusivities $\widetilde{D_x^{eff,co}}$ and $\widetilde{D_y^{eff,co}}$ along the x- and y- directions, respectively, of the columnar grain structure with respect to the effective diffusivity of the equiaxed grain structure. The relative quantities are defined as $D_x^{eff,co}/D_x^{eff,eq}$ and $D_y^{eff,co}/D_x^{eff,eq}$, where $D_x^{eff,co}$, $D_y^{eff,co}$ are the effective diffusivities along the x-, y-directions, respectively, of the columnar grain structure and $D_x^{eff,eq}$ is the effective diffusivity of the equiaxed grain structure. Overall, the figure indicates that effective diffusion along the x-direction of the columnar grain structure is slower than effective diffusion in the equiaxed grain structure, but the y-direction effective diffusion in the columnar grain structure is faster than effective diffusion in the equiaxed grain structure.

These results have two important implications for engineering tunability of ionic transport in polycrystalline LLZO. First, the anisotropy of effective ionic transport can be entirely tailored by microstructural features alone, even if the diffusivities within individual bulk and grain boundary regions are independently isotropic. Second, the anisotropy at a given operating temperature can be tuned by engineering the diffusion properties within the grain boundaries at the atomistic scale since the temperature dependence profile of the anisotropy factor depends on T_e. Note again that the equivalent temperature T_e is determined by inter-relation between intrinsic bulk and grain boundary diffusivities (see Fig. 1c). We emphasize that the effects of the grain morphology are entirely ignored within conventional equivalent circuit models, which considers only the overall grain size or grain boundary fraction rather than shape or distribution. This highlights the distinctive capability of our modeling framework for exploring important mesoscopic features of solid electrolyte grain structures.

Collective impacts of atomic-scale and mesoscopic microstructural properties. Having assessed individual effects of mesoscopic grain structure and atomistic grain boundary structure, we proceed to map the cooperative impacts of both features on ionic conduction behavior. As a representative characteristic, Fig. 6a, b include heat maps examining the critical temperature T_c as functions of D_0^{gb} and E_a^{gb} for selected average grain sizes and grain boundary widths. T_c is useful as a gauge of microstructural sensitivity because it describes the threshold beyond which grain boundary-dominated conduction pathways are observed and contribute strongly to the observed ionic conductivity.

This designability map captures two interesting characteristic behaviors. First, the dependence of T_c on D_0^{gb} is highly non-linear, particularly considering the logarithmic scale of D_0^{gb} axis (Fig. 6a and Supplementary Fig. 5a, b). This trend means that the mechanistic transition point of ionic transport changes more drastically with the prefactor when D_0^{gb} is small. On the other hand, T_c varies almost linearly with E_a^{gb} within the studied range (Supplementary Fig. 5c, d). Second, the variation of T_c is more sensitive to the grain boundary diffusion properties (both D_0^{gb} and E_a^{gb}) for LLZO processed with larger grains or thinner grain boundaries. This is clearly indicated by the largest variation of T_c with D_0^{gb} and when $\langle \widetilde{d} \rangle$ is large or $\langle \widetilde{l_{gb}} \rangle$ is small (see both Fig. 6a, b and Supplementary Fig. 5). This implies that the ionic transport mechanism varies more drastically with the atomic-scale grain boundary properties when the overall grain boundary fraction is smaller, pointing to an interdependence between atomic-scale and mesoscopic grain structural properties. This interdependence can be amplified by the mesoscale microstructure (see Supplementary Fig. 5 and accompanying discussion).

We emphasize that the quantitative variability of T_c in Fig. 6a, b provides guidelines for tuning ionic transport in LLZO by

co-engineering the mesoscopic grain structural topology and atomistic grain boundary structure/chemistry. By controlling these features at both length scales, we may target a critical temperature that lies either within or outside the operating temperature range, depending on whether we wish to incorporate the potential positive or negative effects of the grain boundaries (see blue shaded regions in Supplementary Fig. 5 for example). We can likewise use the designability map to estimate how sensitive the ionic conductivity should be to processing conditions for a given target operating temperature. This exemplifies how a design space can be determined for engineering overall ionic conduction properties of complex solid electrolyte microstructures.

Further practical information can be extracted from the designability map by connecting it directly to the atomically derived statistical distributions shown in Fig. 2. Accordingly, we applied a simple statistical approach to integrate the statistics in Fig. 2 and the predicted T_c presented in Fig. 6a, b. Since a chosen pair (D_0^{gb}, E_a^{gb}) corresponds to a particular T_c, we may assess the relative likelihood of expression of the particular T_c by considering the statistical probabilities of D_0^{gb} and E_a^{gb}. The likelihood for T_c can be simply estimated by computing the joint probability $P(D_0^{gb}, E_a^{gb})$ for the corresponding values of D_0^{gb} and E_a^{gb}. Assuming that D_0^{gb} and E_a^{gb} are independent, the joint probability is computed as $P(D_0^{gb})P(E_a^{gb})$, where $P(D_0^{gb})$ and $P(E_a^{gb})$ are obtained from fitted Gaussian distributions for Fig. 2c, b, respectively. Note that for $P(E_a^{gb})$, we only consider the lower mode (blue curve in Fig. 2b) to avoid atomic trapping.

Figure 6c includes an example of the computed likelihood for T_c for three different grain sizes. In addition to T_c, we apply this approach to the ratio $\sigma^{eff}/\sigma^{bulk}$, where σ^{eff} is the effective ionic conductivity and σ^{bulk} is the bulk ionic conductivity, at a fixed temperature. This quantifies the grain boundary effect on the effective ionic conductivity at a given operating temperature. Figure 6d shows the results for the conductivity ratio at 298 K with different grain sizes. Analogous examples for different grain boundary widths can be found in Supplementary Fig. 6 in Supplementary Note 5. In addition to demonstrating how the statistical information derived from the atomistic simulations can be integrated with the mesoscale simulation results, the analyzed likelihoods have practical implications. The likelihood for T_c (Fig. 6c and Supplementary Fig. 6a) can provide guidance for identifying microstructural features with the best chance of controlling the dominant transport mechanisms within a relevant operating temperature window (e.g., $T_L \le T \le T_H$, marked by the gray shaded region). The likelihood for $\sigma^{eff}/\sigma^{bulk}$ (Fig. 6d and Supplementary Fig. 6b) allows us to determine how much realistic influence grain boundaries might have on the overall ionic transport properties. For instance, the grain boundaries are very probably blocking at 298 K for a relative grain size $\langle \tilde{d} \rangle = 5.6$ since the likelihood is highest for $\sigma^{eff}/\sigma^{bulk} < 1.0$ (to the left of the red dashed line). This blocking tendency clearly decreases for larger grains as the distribution of likelihood shifts towards higher values of $\sigma^{eff}/\sigma^{bulk}$.

This procedure well demonstrates the practicality of the constructed designability map in Fig. 6a, b and illustrates how the statistics from atomistic simulations can be organically coupled with the mesoscopic modeling. However, we caution that the likelihoods in Fig. 6c, d are not comprehensive probabilities, as they do not account for all possible pairs of (D_0^{gb}, E_a^{gb}), but are rather constrained to the sampling area within the designability map in Fig. 6a, b.

DISCUSSION

Beyond fundamental understanding of the microstructure-conductivity relationship (including the origins of empirical trends like the Meyer-Neldel rule), our study has important practical consequences for understanding LLZO performance and durability. The impacts of microstructure increase in magnitude as the operating temperature approaches (or surpasses) the critical temperature T_c, which in turn exhibits high sensitivity to both atomic-scale grain boundary properties and mesoscopic grain structure. The results in Fig. 6, which incorporate microstructural effects at both scales, confirm that electrolyte microstructure could indeed impact ionic conductivity at temperatures relevant for battery operation.

In practice, a wide range of experimental values of the activation barrier E_a for LLZO are reported, depending on specific composition and processing conditions (see Supplementary Table 3 for an extensive list). Our analysis demonstrates that accessible ranges of atomistic grain boundary and mesoscale grain structures can lead to similarly large variability that is effectively captured within the simulations. Furthermore, the experiments show an E_a distribution that is well described by a convolution of two distinct peaks (Fig. 2d), in excellent quantitative agreement with our corresponding distribution from disordered MD simulations. This fits our predictions of a change in the dominant conduction mechanism above T_c, leading us to conclude that the higher-barrier literature reports are dominated by conduction through grain boundaries or similar internal interfaces. In these cases, it can be assumed that the specific chemistries and processing conditions are associated with lower T_c values.

Similarly, while some reports show perfectly linear Arrhenius behavior, many others suggest deviations similar to those predicted in our analysis due to microstructural effects (see Supplementary Table 3). In fact, only 17% of the samples we found from our comprehensive literature analysis were completely Arrhenius. Of the samples that were definitely non-Arrhenius, nearly half (48%) show an increase in E_a with temperature, consistent with the transport mechanism switching to grain boundary dominated pathways. For example, Zhao et al.[67] evaluated the E_a of several samples processed under the same conditions but with different concentrations of aluminum dopant. The Arrhenius plots showed clear changes in slope, with apparent T_c values around room temperature (~313 to 333 K). The slight variation in these values was correlated with dopant concentration—an illustration of the sensitivity of T_c to atomic-scale grain boundary composition, as predicted by our models. Our results also help to explain specific observations of ionic conductivity trends with systematic variation of mesoscale grain structures. For instance, Sakamoto et al.[14] found that compared to solid-state processing, sol-gel processing leads to much smaller grains, resulting in a steeper Arrhenius plot that agrees with our predictions (see Supplementary Fig. 3a in Supplementary Note 2). Moreover, our models allow us to safely conclude that when non-Arrhenius behavior exhibits a trend that is opposite to that predicted from our analysis (e.g., Saccoccio et al.[68], Murugan et al.[69], Rawlence et al.[70], Huang et al.[71]), then it must be attributable to physical factors other than grain boundary mobility or grain structure. Instead, we suggest that these experiments feature temperature-dependent changes in the carrier concentration, correlation factor[72], phase behavior, or microstructure, which are explicitly ignored in our current analysis. We further note that the observation of non-Arrhenius behavior depends on both the operating temperature range and microstructure-dependent T_c, which can explain why the phenomenon is only sometimes observed.

Beyond ionic conductivity, our multiscale simulations also offer potentially valuable insights into the Li dendrite formation that can occur within solid electrolytes and lead to battery failure[16,27,73,74]. In LLZO, dendrite formation has often been observed to occur through grain boundaries[17], while specific grain boundary properties that promote dendrite nucleation/growth have not been pinned down. Dendrites are known to form when

the current density exceeds a critical value. This threshold is characterized by the so-called critical current density (CCD), which is defined as a specific current density above which Li dendrites form during battery operation. At currents above the CCD, transporting Li^+ ions are thought to sufficiently concentrate at the grain boundaries, eventually leading to the formation of continuous, condensed Li metallic phases that percolate through the boundary network although their physical origins still remain elusive. To avoid failure, the battery cell should be operated in such a way that the current density does not exceed the CCD, limiting the performance of the batteries. We argue that the CCD failure is closely related to the relative local diffusion properties of the individual bulk and grain boundary transport channels. As such, we suggest that controlling the critical temperature, T_c, could provide a template for increasing the CCD, thereby allowing for higher current density during battery operation.

More specifically, we hypothesize that for any solid electrolyte, the CCD is determined in large part by the difference between the operating temperature T and the critical temperature T_c. Let us first consider cases for which the grain boundary diffusion is slower than the bulk counterpart ($T < T_c$). In this case, Li^+ ions would mostly transport through bulk, making Li dendrite growth though grain boundaries less likely if other factors (e.g., mechanical interactions[8], grain boundary blocking-induced Li accumulation) are excluded. However, due to low overall ionic conductivity, the performance may be poor. Once the grain boundaries begin to dominate over bulk conduction channels ($T > T_c$), two competing factors can determine Li dendrites formation: 1) concentration of current density at the grain boundaries; and 2) a high average atomic density of mobile Li^+ ions along these boundaries. If the grain boundary diffusion is sufficiently fast, migrating ions will preferentially choose grain boundaries to conduct, concentrating the current density there and potentially promoting dendrite formation. On the other hand, extremely fast diffusion along grain boundaries may result in larger interspacing between the migrating ions owing to their sufficiently facile movement, potentially inhibiting dendrite formation. It is also important to note that variations in the diffusivity in different grain boundaries in the same microstructure will determine which factor dominates locally. In addition, even extremely fast diffusion in some grain boundaries that back-up at junctions or by other obstacles in the microstructure may result in the dendrite formation. We speculate that there exists a certain intermediate temperature range that gives rise to both sufficient concentration of current density at grain boundaries and high enough mobile ion density within these boundaries, such that dendrite initiation will occur unavoidably. This range must lie near T_c, at which grain boundary conduction first begins to dominate.

Although more quantitative analysis is required to support our hypothesis, this line of thinking highlights the potential importance of T_c and its relationship to both microstructure and operating temperature when determining the conditions for Li dendrite growth along grain boundaries. It is worth pointing out that precise correlations between the CCD and grain size of LLZO electrolytes remain inconclusive—with the increasing grain size, conflicting experiments have reported both increasing[16] and decreasing[27] CCD trends. Our results offer possible explanations for this inconsistency. First, the actual LLZO solid electrolyte temperatures during battery operation are different in these experiments, even for similar T_c for the two different measurements. The difference could be attributable to different local thermal transport depending on thermal management within the insulating electrolyte. Second, T_c can be very different for the two cases with similar measurement temperatures. Indeed, as shown in Fig. 6, T_c can significantly vary even for similar grain structures due to subtly different grain boundary diffusion properties. This would alter the interplay between the competing factors explained above and result in different tendencies of the Li dendrite growth along grain boundaries.

In summary, our generalizable multiscale modeling framework combines atomic-scale molecular dynamics simulations, mesoscopic phase-field simulations, and the efficient Fourier-spectral iterative-perturbation method to predict ionic conductivity through polycrystalline solid electrolytes. The framework was applied to investigating the relationship between microstructure and ionic transport in the polycrystalline $Li_{7-x}La_3Zr_2O_{12}$ (LLZO) garnet system using synthetic digital microstructures. Our comprehensive approach provides insights into fundamental properties of conductivity in complex microstructures, allows interpretation of inconsistent literature data, and suggests guidance to engineer LLZO's durability and performance.

The breadth and depth of insights provided from our study demonstrate the benefit of combining predictive simulations at multiple scales into a flexible framework. Unlike previous studies, the diffusion parameters in grain boundary regions were quantified via atomic-scale simulations using many randomly disordered atomistic models, providing a physically motivated database of parameters which capture nontrivial characteristics distinct from bulk transport and show a wide range of local diffusion parameters in the grain boundary regions. Our mesoscale approach also incorporates advantages, combining the efficiency typically associated with equivalent circuit descriptions with the full microstructural complexity inherent in far more expensive direct diffusion simulations. Accordingly, our integrated approach allows for an efficient exploration of a much wider range of the parameter space without loss of microstructural details. Our model highlights the significant dependence of the ionic conductivity on microstructure and grain-boundary diffusivity at battery operating temperatures and also demonstrates the interdependence of these parameters.

Our simulations have advanced fundamental understanding by showing that microstructural features at both the atomistic and mesoscopic scales can make a significant qualitative and quantitative variation in ionic conductivity. The relevance of these predictions is borne out by an extensive literature analysis of LLZO experiments, which show specific signatures of microstructural impacts that our simulations are able to capture. Through our analyses, we propose two descriptors to characterize ionic transport behavior in polycrystalline electrolytes: the equivalent temperature, T_e, at which bulk and grain boundaries feature the same intrinsic ionic diffusivities, and the critical temperature, T_c, above which conduction through the grain boundaries become dominant. Detailed analysis of T_e and T_c for a wide variety of microstructural features and grain boundary diffusivity parameters in LLZO allowed us to unravel the nature of the interdependency of temperature, atomic-scale grain boundary properties, and mesoscale grain structure for the first time. Since the conduction mechanism changes at T_c, operating temperatures near T_c can cause ionic conductivity to vary significantly during operation. In addition, grain size and grain boundary width can have opposite effects on the effective ionic conductivity depending on whether the operating temperature is above or below T_c. In turn, our results also verify that changing grain size and/or grain boundary width can significantly change T_c, meaning the experimentally measured sensitivity of ionic conductivity to temperature could be different depending on sample preparation, microstructure, and measurement temperatures. This understanding provides insight into the origin of inconsistency in literature-reported experiments. Grain morphology is also found to be important, with temperature-dependent anisotropic diffusivity emerging from intrinsically isotropic transport when columnar grains are present. Finally, our results also offer an additional interpretation of the well-known Meyer-Neldel rule[64–66], which predicts a linear relationship between log (D_0) and E_a for ionic conductivity in solid electrolytes. Whereas the rule is generally associated with bulk transport

mechanisms, we show that the same behavior is also observed at the mesoscopic microstructure-level (Fig. 4c, f).

More broadly, our results have practical implications for predicting and improving solid-state battery performance and durability. In particular, our analysis points to the possibility of using microstructural features—mesoscopic grain structural topology, as well as atomistic grain boundary structure and composition—to tune ionic conductivity. Accordingly, we introduced a designability map of Li^+ ion transport within polycrystalline LLZO, detailing which atomistic and mesoscopic parameters of the solid electrolyte can be selected for achieving the targeted performance under given operating conditions. We point out that these multiscale aspects can be practically engineered. First, the atomistic grain boundary structure and property can be controlled by grain boundary segregation of chemical dopants[61] or thermally induced structural transformations[75]. Note that the wide range of grain boundary diffusion parameters in our atomistic simulations indicates the possibility of high designability at the atomic scale. Second, the mesoscopic topological features such as grain size, grain boundary width, and grain morphology of the solid electrolyte microstructure can be varied by thermal and/or mechanical processing conditions during sintering. For instance, such topological variability can be generally found in ceramic microstructures produced by solid-state synthesis[16], thin film growth[76,77], and 3D printing[78,79]. Third, the battery operating conditions can be optimized to effectively take advantage of the microstructural impacts because the positive or negative roles of grain boundary transport contributions depend on the operating temperature with relation to the critical temperature. The temperature of a solid electrolyte with a specific microstructure—and hence a specific T_c, could therefore be locally controlled to maximize the contribution of fast grain boundary conduction to overall ionic transport, while sufficiently suppressing Li accumulation at grain boundaries.

It is worth noting that our modeling framework can be extended to account for more realistic features to improve the practicality of the integrated model. For example, we may explicitly incorporate the effects of dopants, which are usually added to LLZO for controlling the phase stability and sintering conditions[11,12]. Since the dopants are known to segregate to grain boundaries, non-trivial variation of grain boundary properties is expected, which can be investigated by systematically designed atomistic simulations. For the mesoscale modeling approach, the parameterization of the position-dependent diffusivity model (Eq. (3)) can be improved by implementing more realistic description based on statistical sampling of the grain boundary diffusion parameters D_0^{gb} and E_a^{gb}. This may require introducing the stochastic equation incorporating the statistical information of individual D_0^{gb} and E_a^{gb} shown in Fig. 2.

Overall, our results provide an important step towards establishing the significance of microstructure for ion conduction in garnets and related oxide-based solid-state electrolytes. As a result, our work could form the basis of a template for ultimately connecting ceramic processing conditions to performance. We emphasize that although our attention was confined to a specific, single-phase electrolyte material, the described multiscale modeling framework and analytical approach should be generally applicable to any polycrystalline, porous, multi-particle, or multi-phase solid-state ionic conductors provided suitable atomistic models can be introduced, opening use to a wide variety of potential energy applications.

METHODS

Fourier-spectral iterative perturbation method

To obtain the steady-state Li^+ composition profile by numerically solving Eq. (2), we split our position-dependent diffusivity function into homogeneous ($\overline{D}_{ij}$) and perturbation ($\Delta D_{ij}(\vec{\mathbf{r}})$) parts: $D_{ij}(\vec{\mathbf{r}}) = \overline{D}_{ij} + \Delta D_{ij}(\vec{\mathbf{r}})$. In addition, the composition gradient also splits into homogeneous and perturbation parts as:

$$q_j(\vec{\mathbf{r}}) \equiv \nabla_j X(\vec{\mathbf{r}}) = \nabla_j \overline{X} + \nabla_j \delta X = \overline{q}_j + \delta q_j(\vec{\mathbf{r}}), \tag{6}$$

where we define $\overline{q}_j \equiv \nabla_j \overline{c}$ and $\delta q_j(\vec{\mathbf{r}}) \equiv \nabla_j \delta X$. Therefore, Eq. (2) can be rearranged to $\overline{D}_{ij}\nabla_i \cdot \nabla_j \delta X = -\nabla_i \cdot \left[\Delta D_{ij}(\vec{\mathbf{r}})\left\{\overline{q}_j + \nabla_j \delta X\right\}\right]$. Taking the Fourier transform of this equation, we obtain the equation in k-space: $-\overline{D}_{ij}k_i k_j [\delta X]_k = -J \cdot k_i \left[\Delta D_{ij}(\vec{\mathbf{r}})\left\{\overline{q}_j + \left[J \cdot k_j [\delta X]_k\right]_r\right\}\right]_k$, where k_i represents the reciprocal vector, J is $\sqrt{-1}$, $[\,]_k$ represents the Fourier transform, and $[\,]_r$ represents the inverse Fourier transform. For the periodic boundary condition for δX due to the Fourier spectral method, the condition for the perturbation part of the composition: $\int_{\partial\Omega}[\nabla_j \delta X] n_i da = 0$ is satisfied, where n_i represents a normal vector to the computational domain surface $\partial\Omega$. When $\overline{D}_{ij}k_i k_j \neq 0$, the transformed algebraic equation in k-space is rearranged as the following: $[\delta X]_k = (J \cdot k_i [\Delta D_{ij}(\vec{\mathbf{r}})\{\overline{q}_j + [J \cdot k_j [\delta X]_k]_r\}]_k)/(\overline{D}_{ij}k_i k_j)$. On the other hand, when $\overline{D}_{ij}k_i k_j = 0$, we set the solution as $[\delta X]_k = 0$ since the solvability condition: $(1/V_\Omega)\int_\Omega \left\{-\nabla_i \cdot \left[\Delta D_{ij}(\vec{\mathbf{r}})\left\{\overline{q}_j + \nabla_j \delta X\right\}\right]\right\} dV = 0$ is satisfied, where V_Ω is the volume of the computational domain Ω, according to *i*) the periodic boundary condition for δX; *ii*) the divergence theorem for the condition $\int_{\partial\Omega}[\nabla_j \delta X] n_i da = 0$; and *iii*) the steady-state condition: $(1/V_\Omega)\int_\Omega \left\{\nabla_i \cdot \left[D_{ij}(\vec{\mathbf{r}})\right] \nabla_j X\right\} dV = 0$. By employing the fixed-point iteration scheme[80] for this algebraic equation in k-space with the convergence condition: $\sqrt{(1/V_\Omega)\int_\Omega \{X_{n+1} - X_n\}^2 dV} < \epsilon$, we obtain the converged δX (*i.e.*, $X = \overline{X} + \delta X$) within the given complex microstructure. Note that the homogeneous part $\overline{q}_j$ of the composition gradient field is the macroscopic composition gradient, which remains constant during iterations and acts as a boundary condition for Eq. (2).

Molecular dynamics simulations

The cubic phase of LLZO[9,43,81] was studied using the classical molecular dynamics software LAMMPS[82]. The interatomic potentials were adopted from the study by Kozinsky et al.[50]. For simplicity, we did not explicitly consider dopant atoms, but instead simulated their effects by introducing vacancies in undoped cubic LLZO. Disordered systems were used to obtain diffusion parameters for the grain boundary regions. These models were generated using a melt-and-quench approach from a 3000 K simulation, with that temperature chosen to incorporate significant disorder while retaining the local structure of the cation-oxygen cages. The generation of $2 \times 2 \times 2$ supercells with three lithium concentrations of $Li_{6.25}La_3Zr_2O_{12}$, $Li_{6.5}La_3Zr_2O_{12}$, and $Li_{6.75}La_3Zr_2O_{12}$ is discussed in Supplementary Note 3. For each lithium concentration, two cell densities were simulated to investigate the effects of density on diffusion. Details on the density of each simulation, disordered and crystalline, is given in Supplementary Note 3. Pair distribution functions for all simulations are also shown in Supplementary Fig. 4, along with a discussion of key structural features for each disordered model.

Diffusion parameters for the crystalline and disordered systems were obtained by classical molecular dynamics (CMD) $2 \times 2 \times 2$ supercells containing 1488–1520 atoms using the canonical (*NVT*) ensemble and a Nose-Hover thermostat. Long-range Coulomb interactions were solved using Ewald summation with a cutoff radius of 8 Å. All systems were run for 6 ns with a 1 fs time step at 700–1700 K in increments of 200 K to obtain diffusion parameters, using the last 5 ns for analysis. Diffusion coefficients were determined by linearly fitting the slopes of the mean squared displacement of Li-ions. Activation energies (E_a) were calculated by fitting Arrhenius plots of diffusion using all simulated temperatures.

Methods for determining T_e and T_c

The equivalent temperature (T_e) can easily be derived by equating two Arrhenius equations for grain and grain boundary diffusivities (i.e., Eq. (4)) by the definition of T_e at which the two diffusivities are equal. Therefore, it is expressed as: $T_e = [E_a^{gb} - E_a^{bulk}]/[k_B \ln(D^{gb,0}/D^{bulk,0})]$. On the other hand, the critical temperature (T_c) needs to be determined by a numerical fitting procedure for the computed effective ionic conductivities (σ_{eff}) (or effective diffusivities) as a function of temperature since the corresponding analytical expression is not available. Since T_c characterizes the mechanistic transition from grain- to grain boundary-dominated conduction mode in the computed effective conductivity, we obtain two distinct linear fitting curves for the two mechanistic regimes. The two mechanistic regimes can easily be identified by analyzing the slopes of linear regimes of log

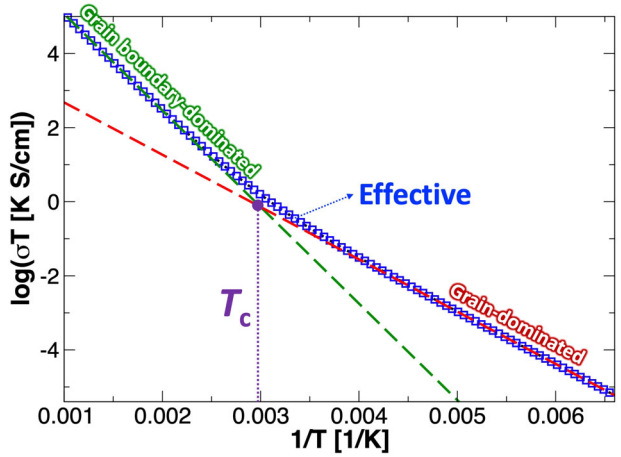

Fig. 7 Graphical representation of the numerical procedure for determining the critical temperature (T_c). Systematic determination of T_c for the mechanistic transition between grain- and grain boundary-dominated conduction modes in the computed effective ionic conductivity.

($\sigma_{\mathrm{eff}}T$) at low and high temperatures and comparing them with the intrinsic grain and grain boundary diffusion activation energies (i.e., $-E_a^{\mathrm{bulk}}/k_B$ and $-E_a^{\mathrm{gb}}/k_B$, where E_a^{bulk} is the activation energy for diffusion in grain interior, E_a^{gb} is the activation energy for diffusion in grain boundary, and k_B is the Boltzmann constant) as shown in Fig. 7 (also, see Fig. 1c in the main text). T_c is then obtained by equating the two linear fitting functions.

DATA AVAILABILITY

The data that support the findings of this study are available from the corresponding authors upon reasonable request.

CODE AVAILABILITY

The code used to calculate the results of this study are available from the corresponding authors upon reasonable request. Some restriction may apply due to authors' institutional guidelines.

Received: 25 May 2021; Accepted: 16 November 2021;
Published online: 21 December 2021

REFERENCES

1. Stramare, S., Thangadurai, V. & Weppner, W. Lithium lanthanum titanates: a review. *Chem. Mater.* **15**, 3974–3990 (2003).
2. Knauth, P. Inorganic solid Li ion conductors: an overview. *Solid State Ion.* **180**, 911–916 (2009).
3. Cussen, E. J. Structure and ionic conductivity in lithium garnets. *J. Mater. Chem.* **20**, 5167–5173 (2010).
4. Thangadurai, V., Narayanan, S. & Pinzaru, D. Garnet-type solid-state fast Li ion conductors for Li batteries: critical review. *Chem. Soc. Rev.* **43**, 4714–4727 (2014).
5. Bachman, J. C. et al. Inorganic solid-state electrolytes for lithium batteries: mechanisms and properties governing ion conduction. *Chem. Rev.* **116**, 140–162 (2016).
6. Gao, Y. et al. Classical and emerging characterization techniques for investigation of ion transport mechanisms in crystalline fast ionic conductors. *Chem. Rev.* **120**, 5954 (2020).
7. Monroe, C. & Newman, J. The impact of elastic deformation on deposition kinetics at lithium/polymer interfaces. *J. Electrochem. Soc.* **152**, A396–A404 (2005).
8. Barai, P., Higa, K., Ngo, A. T., Curtiss, L. A. & Srinivasan, V. Mechanical stress induced current focusing and fracture in grain boundaries. *J. Electrochem. Soc.* **166**, A1752–A1762 (2019).
9. Murugan, R., Thangadurai, V. & Weppner, W. Fast lithium ion conduction in Garnet-type $Li_7La_3Zr_2O_{12}$. *Angew. Chem. Int. Ed.* **46**, 7778–7781 (2007).
10. Kumazaki, S. et al. High lithium ion conductive $Li_7La_3Zr_2O_{12}$ by inclusion of both Al and Si. *Electrochem. Commun.* **13**, 509–512 (2011).
11. Rangasamy, E., Wolfenstine, J. & Sakamoto, J. The role of Al and Li concentration on the formation of cubic garnet solid electrolyte of nominal composition $Li_7La_3Zr_2O_{12}$. *Solid State Ion* **206**, 28–32 (2012).
12. Miara, L. J. et al. Effect of Rb and Ta doping on the ionic conductivity and stability of the Garnet Li 7 + 2 x − y(La 3 − xRb x)(Zr 2 − yTa y)O 12(0 ≤ x ≤ 0.375, 0 ≤ y ≤ 1) superionic conductor: a first principles investigation. *Chem. Mater.* **25**, 3048–3055 (2013).
13. Zhang, Y. H. et al. Effect of lithium ion concentration on the microstructure evolution and its association with the ionic conductivity of cubic garnet-type nominal Li7Al0.25La3Zr2O12 solid electrolytes. *Solid State Ion* **284**, 53–60 (2016).
14. Sakamoto, J., Rangasamy, E., Kim, H., Kim, Y. & Wolfenstine, J. Synthesis of nanoscale fast ion conducting cubic $Li_7La_3Zr_2O_{12}$. *Nanotechnology* **24**, 8 (2013).
15. Tenhaeff, W. E. et al. Resolving the grain boundary and lattice impedance of hot-pressed $Li_7La_3Zr_2O_{12}$ Garnet electrolytes. *Chemelectrochem* **1**, 375–378 (2014).
16. Sharafi, A., Haslam, C. G., Kerns, R. D., Wolfenstine, J. & Sakamoto, J. Controlling and correlating the effect of grain size with the mechanical and electrochemical properties of $Li_7La_3Zr_2O_{12}$ solid-state electrolyte. *J. Mater. Chem. A Mater. Energy Sustain* **00**, 1–14 (2017).
17. Cheng, E. J., Sharafi, A. & Sakamoto, J. Intergranular Li metal propagation through polycrystalline Li6.25Al0.25La3Zr2O12 ceramic electrolyte. *Electrochim. Acta* **223**, 85–91 (2017).
18. Chen, L. Q. & Yang, W. Computer-simulation of the domain dynamics of a quenched system with a large number of nonconserved order parameters - the grain-growth kinetics. *Phys. Rev. B* **50**, 15752–15756 (1994).
19. Krill, C. E. & Chen, L. Q. Computer simulation of 3-D grain growth using a phase-field model. *Acta Mater.* **50**, 3057–3073 (2002).
20. Dawson, J. A., Canepa, P., Famprikis, T., Masquelier, C. & Islam, M. S. Atomic-scale influence of grain boundaries on Li-ion conduction in solid electrolytes for all-solid-state batteries. *J. Am. Chem. Soc.* **140**, 362–368 (2018).
21. Tian, H. K., Liu, Z., Ji, Y. Z., Chen, L. Q. & Qi, Y. Interfacial electronic properties dictate Li dendrite growth in solid electrolytes. *Chem. Mater.* **31**, 7351–7359 (2019).
22. Yu, H. C., Choe, M. J., Amatucci, G. G., Chiang, Y. M. & Thornton, K. Smoothed boundary method for simulating bulk and grain boundary transport in complex polycrystalline microstructures. *Comput. Mater. Sci.* **121**, 14–22 (2016).
23. Hu, J. M. et al. Phase-field based multiscale modeling of heterogeneous solid electrolytes: applications to nanoporous Li3PS4. *Acs Appl. Mater. Interfaces* **9**, 33341–33350 (2017).
24. Cahn, J. W. & Hilliard, J. E. Free energy of a nonuniform system .1. Interfacial free energy. *J. Chem. Phys.* **28**, 258–267 (1958).
25. Allen, S. M. & Cahn, J. W. Microscopic theory for antiphase boundary motion and its application to anti phase domain coarsening. *Acta Metall.* **27**, 1085–1095 (1979).
26. Cheng, L. et al. The origin of high electrolyte-electrode interfacial resistances in lithium cells containing garnet type solid electrolytes. *Phys. Chem. Chem. Phys.* **16**, 18294–18300 (2014).
27. Cheng, L. et al. Effect of surface microstructure on electrochemical performance of Garnet solid electrolytes. *ACS Appl. Mater. Interfaces* **7**, 2073–2081 (2015).
28. Cheng, L. et al. Interrelationships among Grain size, surface composition, air stability, and interfacial resistance of Al-substituted Li 7La 3Zr 2O 12 solid electrolytes. *ACS Appl. Mater. Interfaces* **7**, 17649–17655 (2015).
29. Biswas, S., Schwen, D., Wang, H., Okuniewski, M. & Tomar, V. Phase field modeling of sintering: Role of grain orientation and anisotropic properties. *Comput. Mater. Sci.* **148**, 307–319 (2018).
30. Abdeljawad, F. et al. Sintering processes in direct ink write additive manufacturing: a mesoscopic modeling approach. *Acta Mater.* **169**, 60–75 (2019).
31. Hotzer, J., Seiz, M., Kellner, M., Rheinheimer, W. & Nestler, B. Phase-field simulation of solid state sintering. *Acta Mater.* **164**, 184–195 (2019).
32. Shi, R., Wood, M., Heo, T. W., Wood, B. C. & Ye, J. Towards understanding particle rigid-body motion during solid-state sintering. *J. Eur. Ceram. Soc.* **41**, 211–231 (2021).
33. Wolfenstine, J., Sakamoto, J. & Allen, J. L. Electron microscopy characterization of hot-pressed Al substituted $Li_7La_3Zr_2O_{12}$. *J. Mater. Sci.* **47**, 4428–4431 (2012).
34. Vikrant, K. S. N. & Garcia, R. E. Charged grain boundary transitions in ionic ceramics for energy applications. *Npj Comput. Mater.* **5**, 12 (2019).
35. Luo, J. Interfacial engineering of solid electrolytes. *J. Mater.* **1**, 22–32 (2015).
36. Guo, X. & Maier, J. Grain boundary blocking effect in zirconia: a Schottky barrier analysis. *J. Electrochem. Soc.* **148**, E121–E126 (2001).
37. Chiang, Y. M., Birnie, D. P. & Kingery, W. D. *Physical Ceramics: Principles for Ceramic Science and Engineering*. (Wiley, 1996).
38. Murch, G. E. The Haven ratio in fast ionic conductors. *Solid State Ion.* **7**, 177–198 (1982).
39. Zhu, J. Z., Chen, L. Q., Shen, J. & Tikare, V. Computing the effective diffusivity using a spectral method. *Mater. Sci. Eng. Struct. Mater. Prop. Microstruct. Process.* **311**, 135–141 (2001).

40. Zhu, J. H., Chen, L. Q., Shen, J. & Tikare, V. Microstructure dependence of diffusional transport. *Comput. Mater. Sci.* **20**, 37–47 (2001).
41. Song, P. C. et al. A comparison of Fourier spectral iterative perturbation method and finite element method in solving phase-field equilibrium equations. *Commun. Comput. Phys.* **21**, 1325–1349 (2017).
42. Li, Y., Wang, Z., Li, C., Cao, Y. & Guo, X. Densification and ionic-conduction improvement of lithium garnet solid electrolytes by flowing oxygen sintering. *J. Power Sources* **248**, 642–646 (2014).
43. Buschmann, H. et al. Structure and dynamics of the fast lithium ion conductor "$Li_7La_3Zr_2O_{12}$". *Phys. Chem. Chem. Phys.* **13**, 19378–19392 (2011).
44. Shen, F. Y., Dixit, M. B., Xiao, X. H. & Hatzell, K. B. Effect of pore connectivity on Li dendrite propagation within LLZO electrolytes observed with synchrotron X-ray tomography. *ACS Energy Lett.* **3**, 1056–1061 (2018).
45. Wachter-Welzl, A. et al. The origin of conductivity variations in Al-stabilized $Li_7La_3Zr_2O_{12}$ ceramics. *Solid State Ion.* **319**, 203–208 (2018).
46. Smetaczek, S. et al. Local Li-ion conductivity changes within Al stabilized $Li_7La_3Zr_2O_{12}$ and their relationship to three-dimensional variations of the bulk composition. *J. Mater. Chem. A* **7**, 6818–6831 (2019).
47. Mukhopadhyay, S., Thompson, T. & of, J. S. C. Structure and stoichiometry in supervalent doped $Li_7La_3Zr_2O_{12}$. *J. Am. Chem. Soceity* **27**, 3658–3665 (2015).
48. Meier, K., Laino, T. & Curioni, A. Solid-state electrolytes: revealing the mechanisms of Li-ion conduction in tetragonal and cubic LLZO by first-principles calculations. *J. Phys. Chem. C.* **118**, 6668–6679 (2014).
49. Yu, S. & Siegel, D. J. Grain boundary contributions to Li-ion transport in the solid electrolyte Li 7La 3Zr 2O 12(LLZO). *Chem. Mater.* **29**, 9639–9647 (2017).
50. Kozinsky, B. et al. Effects of sublattice symmetry and frustration on ionic transport in Garnet solid electrolytes. *Phys. Rev. Lett.* **116**, 055901 (2016).
51. Zhu, Y. *Atomistic Modeling of Solid Interfaces in All-solid-state Li-ion Batteries* Ph.D. thesis (University of Maryland, 2018).
52. Shiiba, H. et al. Molecular dynamics studies on the lithium ion conduction behaviors depending on tilted grain boundaries with various symmetries in Garnet-type $Li_7La_3Zr_2O_{12}$. *J. Phys. Chem. C.* **122**, 21755–21762 (2018).
53. Porter, D. A., Easterling, K. E. & Sherif, M. *Phase Transformations in Metals and Alloys (Revised Reprint)*. (CRC Press, 2009).
54. Zhu, Y. S. et al. Dopant-dependent stability of Garnet solid electrolyte interfaces with lithium metal. *Adv. Energy Mater.* **9**, 11 (2019).
55. An, J. et al. Grain boundary blocking of ionic conductivity in nanocrystalline yttria-doped ceria thin films. *Scr. Materialia* **104**, 45–48 (2015).
56. Lin, Y., Fang, S. M., Su, D., Brinkman, K. S. & Chen, F. L. Enhancing grain boundary ionic conductivity in mixed ionic-electronic conductors. *Nat. Commun.* **6**, 9 (2015).
57. Tang, M., Carter, W. C. & Cannon, R. M. Grain boundary transitions in binary alloys. *Phys. Rev. Lett.* **97**, 4 (2006).
58. Tang, M., Carter, W. C. & Cannon, R. M. Diffuse interface model for structural transitions of grain boundaries. *Phys. Rev. B* **73**, 14 (2006).
59. Zhang, H., Srolovitz, D. J., Douglas, J. F. & Warren, J. A. Grain boundaries exhibit the dynamics of glass-forming liquids. *Proc. Natl Acad. Sci. USA* **106**, 7735–7740 (2009).
60. Shimonishi, Y. et al. Synthesis of garnet-type Li7 − xLa3Zr2O12 − 1/2x and its stability in aqueous solutions. *Solid State Ion.* **183**, 48–53 (2011).
61. Zhang, Y. et al. Li+ transport channel size governing Li+ migration in garnet-based all-solid-state lithium batteries. *J. Alloy. Compd.* **767**, 899–904 (2018).
62. Ye, J. C. et al. Amorphization as a pathway to fast charging kinetics in atomic layer deposition-derived titania films for lithium ion batteries. *Chem. Mater.* **30**, 8871–8882 (2018).
63. Wang, Y. et al. Design principles for solid-state lithium superionic conductors. *Nat. Mater.* **14**, 1026–102 (2015).
64. Jackson, W. B. Connection between the Meyer-Neldel relation and multiple-trapping transport. *Phys. Rev. B* **38**, 3595–3598 (1988).
65. Ngai, K. L. Meyer-Neldel rule and anti Meyer-Neldel rule of ionic conductivity - conclusions from the coupling model. *Solid State Ion.* **105**, 231–235 (1998).
66. Muy, S. et al. Lithium conductivity and Meyer-Neldel rule in Li3PO4-Li3VO4-Li4GeO4 lithium superionic conductors. *Chem. Mater.* **30**, 5573–5582 (2018).
67. Zhao, P. C. et al. Self-consolidation mechanism and its application in the preparation of Al-doped cubic $Li_7La_3Zr_2O_{12}$. *Mater. Des.* **139**, 65–71 (2018).
68. Saccoccio, M. et al. Low temperature pulsed laser deposition of garnetLi6.4-La3Zr1.4Ta0.6O12 films as all solid-state lithium battery electrolytes. *J. Power Sources* **365**, 43–52 (2017).
69. Murugan, R., Ramakumar, S. & Janani, N. High conductive yttrium doped $Li_7La_3Zr_2O_{12}$ cubic lithium garnet. *Electrochem. Commun.* **13**, 1373–1375 (2011).
70. Rawlence, M., Garbayo, I., Buecheler, S. & Rupp, J. L. M. On the chemical stability of post-lithiated garnet Al-stabilized $Li_7La_3Zr_2O_{12}$ solid state electrolyte thin films. *Nanoscale* **8**, 14746–14753 (2016).
71. Huang, X. et al. Method using water-based solvent to prepare $Li_7La_3Zr_2O_{12}$ solid electrolytes. *Acs Appl. Mater. Interfaces* **10**, 17147–17155 (2018).
72. Morgan, B. J. Lattice-geometry effects in garnet solid electrolytes: a lattice-gas Monte Carlo simulation study. *R. Soc. Open Sci.* **4**, 21 (2017).
73. Ren, Y. Y., Shen, Y., Lin, Y. H. & Nan, C. W. Direct observation of lithium dendrites inside garnet-type lithium-ion solid electrolyte. *Electrochem. Commun.* **57**, 27–30 (2015).
74. Sharafi, A., Meyer, H. M., Nanda, J., Wolfenstine, J. & Sakamoto, J. Characterizing the Li-$Li_7La_3Zr_2O_{12}$ interface stability and kinetics as a function of temperature and current density. *J. Power Sources* **302**, 135–139 (2016).
75. Meiners, T., Frolov, T., Rudd, R. E., Dehm, G. & Liebscher, C. H. Observations of grain-boundary phase transformations in an elemental metal. *Nature* **579**, 375–37 (2020).
76. Barranco, A., Borras, A., Gonzalez-Elipe, A. R. & Palmero, A. Perspectives on oblique angle deposition of thin films: From fundamentals to devices. *Prog. Mater. Sci.* **76**, 59–153 (2016).
77. Ohring, M. & Knovel. *Materials Science of Thin Films*. (Elsevier Science, 2002).
78. Chen, Z. W. et al. 3D printing of ceramics: a review. *J. Eur. Ceram. Soc.* **39**, 661–687 (2019).
79. McOwen Dennis, W. et al. 3D-printing electrolytes for solid-state batteries. *Adv. Mater.* **30**, 1707132 (2018).
80. Burden, R. L. & Faires, J. D. *Numerical Analysis*. (Brooks/Cole, 2001).
81. Wolfenstine, J., Allen, J. L., Read, J. & Sakamoto, J. Chemical stability of cubic $Li_7La_3Zr_2O_{12}$ with molten lithium at elevated temperature. *J. Mater. Sci.* **48**, 5846–5851 (2013).
82. Plimpton, S. Fast parallel algorithms for short-range molecular dynamics. *J. Comput. Phys.* **117**, 1–19 (1995).
83. Towns, J. et al. XSEDE: accelerating scientific discovery. *Comput. Sci. Eng.* **16**, 62–74 (2014).

ACKNOWLEDGEMENTS

This work was performed under the auspices of the U.S. Department of Energy by Lawrence Livermore National Laboratory under Contract DE-AC52-07NA27344. The authors acknowledge financial support from the U.S. Department of Energy (DOE), Office of Energy Efficiency and Renewable Energy, Vehicle Technologies Office, through the Battery Materials Research program. This work was partially funded by the Laboratory Directed Research and Development Program at LLNL under the project tracking code 15-ERD-022 and 18-FS-019. Additional computing support came from the LLNL Institutional Computing Grand Challenge program. The work of A. Grieder and N. Adelstein was supported by the National Science Foundation under Grant No. DMR-1710630 and simulations utilized the Extreme Science and Engineering Discovery Environment (XSEDE)[83] Stampede2 at the University of Texas, Austin through allocation DMR180033. Work at The Pennsylvania State University is partially supported by the Donald W. Hamer Foundation through a Hamer Professorship. Helpful discussions about experimental microstructures of solid electrolytes with J. Ye (LLNL) are acknowledged.

AUTHOR CONTRIBUTIONS

T.W.H., N.A. and B.C.W. conceived and designed the study. T.W.H. and B.W. performed mesoscale modeling and microstructure-aware effective ionic conductivity calculations. A.G. performed atomistic simulations and related analysis under the guidance of N.A. and B.C.W. M.W. conducted the comprehensive literature data analysis. T.H. conducted the statistical analysis for connecting atomistic and mesoscale simulation/calculation results. All authors commented on the manuscript and contributed to its final version.

COMPETING INTERESTS

The authors declare no competing interests.

ADDITIONAL INFORMATION

Supplementary information The online version contains supplementary material available at https://doi.org/10.1038/s41524-021-00681-8.

Correspondence and requests for materials should be addressed to Tae Wook Heo, Nicole Adelstein or Brandon C. Wood.